Appl. Phys. B 74, 35–42 (2002)
DOI: 10.1007/s003400100764

Applied Physics B
Lasers and Optics

N.D. NGUYEN
M. SCHMEITS✉

The photorefractive effect at large modulation depth in semiconductors with multiple defect levels

Institute of Physics, University of Liège, 4000 Sart-Tilman, Liège 1, Belgium

Received: 14 August 2001/Revised version: 16 October 2001
Published online: 29 November 2001 • **© Springer-Verlag 2001**

ABSTRACT The photorefractive effect in semiconducting materials with multiple defects is studied in the case of modulation depth $m = 1$. The basic equations are Poisson's equation and the continuity equations for electrons, holes and occupied defect levels. They include all recombination and optical generation mechanisms between the defect levels and valence and conduction bands. Their explicit numerical solution yields microscopic quantities such as space- and time-dependent electrical field profiles, carrier concentrations, as well as generation and recombination rates. The fundamental Fourier component of the electric field yields the two-wave-mixing gain. Application is made for InP with two levels in the forbidden gap, for which steady-state and transient resulting quantities are shown. The resulting features at large modulation depth are of non-sinusoidal shape. Due to the complexity of the system, the final results strongly depend on all parameters intervening in the models used, as is illustrated for several typical cases.

PACS 42.65.Hw; 42.70.Nq; 61.72.Ji

1 Introduction

During the last two decades, the study of the photorefractive effect in semiconducting materials has received much interest [1–3]. The fundamental mechanism at the origin of the photorefractive effect is directly related to the basic properties of the host material and of the introduced impurity atoms. The effect results from the build-up of a space-charge field, initiated by the optical absorption of an interference pattern, followed by transport and capture by defects. The steady-state and transient behavior of the space-charge field determines the device performance in numerous applications, among which holographic storage, optical signal processing and optical circuits are the most important ones.

Most of the observed phenomena are explained by a single-defect model, starting from the set of basic equations established by Kukhtarev [4, 5] in the 1970s. Real crystals, however, may contain more than one impurity level in the forbidden gap. These may be due to intrinsic defects due to some compensation process, to excited levels related to a given impurity species or defects related to the introduction of several impurity atoms. Experimental results obtained for crystals such as $BaTiO_3$, $LiNbO_3$ or InP were interpreted with the existence of multiple defects [6–9]. The presence of at least one additional defect state in the forbidden gap may give rise to several new processes, in addition to those which occur in the single-defect case. The new thermal equilibrium Fermi energy will change the thermal equilibrium occupation of the levels, thus modifying the absorption and recombination rates and yielding space-charge distributions and space-charge fields different from those of the single-defect case. Due to the new absorption processes, additional transport by electrons and holes may be possible. Only in some cases will the effect of the two types of impurities be simply additive. As a final result, the steady-state and transient photorefractive gain and diffraction efficiency may be affected. The transient response under illumination or extinction may not be described by a simple exponential function; the explicit form depends on the time dependence of the various trap filling or emptying processes.

The inclusion of multiple defects in the basic equations has been treated by several authors [6–14]. But, in these treatments, several assumptions were made in order to transform the complex system of equations into expressions which finally could be handled in analytical form. The main assumptions were on low modulation depth and on the quasi-steady-state approximations where electron and hole concentrations are supposed to be constant with time, yielding results in terms of the zeroth- and first-order Fourier terms of the space-charge field only.

The numerical analysis which is proposed here and illustrated by the case of two defect states starts from the basic semiconductor equations, i.e. Poisson's equation and the continuity equations for electrons, holes and occupied levels of both types. All recombination and optical generation terms between the defect levels and the valence and conduction bands are included. These equations are solved numerically, without any approximation, applying techniques which are currently used in the simulation of electronic devices [15]. As a result, one obtains the steady-state and transient response of the photorefractive crystal. The input parameters correspond to the microscopic properties of the host crystal (gap, carrier mobilities, effective masses), the impurities (energy level, concentration, optical and thermal capture cross section) and

✉ Fax: +32-4/366-2990, E-mail: m.schmeits@ulg.ac.be

the experimental conditions (temperature, illumination pattern and applied electric field). The outputs are the electric potential and space-charge field, the free carrier and occupied defect concentrations and the charge density obtained for all modulation depths. From these, the experimentally observed quantities, such as the two-wave-mixing gain coefficient Γ or the diffraction efficiency η under steady-state and transient conditions, are obtained. In such a complex system, where the active defect levels yield intermediate steps in the writing, extinction or erasure processes, a complete numerical modeling allows us to determine the effect of each input parameter on the resulting macroscopic quantities, which are measured in an experiment. Each step can be analyzed in detail, from the photocarrier generation, to transport, carrier redistribution between the various defect levels and final build-up of the space-charge field. Numerical solution of the basic equations in the single-defect, large-modulation case has been reported e.g. by Wolffer et al. [16] and by Singh et al. [17].

The paper is organized as follows: in Sect. 2, we recall the complete set of basic equations underlying the numerical modeling and give the procedure used to integrate these equations. In Sect. 3, we show typical results corresponding to the steady-state application in InP with two defect levels in the forbidden gap. Section 4 discusses cases of transient analysis in the same system and Sect. 5 summarizes and concludes the paper.

2 Basic formalism

The system under study is a homogeneous crystal at a given temperature T. The spatial interference of two coherent beams forms an illumination grating given by

$$I = I_0(1 + m\cos(Kx)) , \tag{1}$$

where I_0 is the intensity amplitude, m is the modulation index and $K = 2\pi/\Lambda$ is the spatial frequency. The fringe spacing Λ is related to the vacuum wavelength λ and incidence angle θ by $\Lambda = \lambda/2\sin\theta$. The system is supposed to be one-dimensional; absorption effects in the perpendicular z direction are therefore neglected.

The crystal is supposed to have two defect states in the forbidden gap. Their energy positions will be labeled $E_{t\mathrm{A}}$ and $E_{t\mathrm{B}}$ respectively, their total concentrations $N_{t\mathrm{A}}$ and $N_{t\mathrm{B}}$ and the concentrations of electrons occupying these levels $n_{t\mathrm{A}}$ and $n_{t\mathrm{B}}$. These defect levels are either of acceptor or of donor type. A state is called acceptor-like when neutral if empty, and negatively charged when occupied; a state is called donor-like when neutral if it is occupied and positively charged when empty. The corresponding contribution to the charge concentration is therefore $qC_t^* = -qn_t$ for an acceptor defect and $qC_t^* = q(N_t - n_t)$ for a donor defect, q being the electronic charge.

The electric potential ψ satisfies Poisson's equation

$$\varepsilon\frac{\partial^2\psi}{\partial x^2} = q\,(n - p - C_t^* + N_{\mathrm{sA}} - N_{\mathrm{sD}}) , \tag{2}$$

where n is the electron concentration, p is the hole concentration and N_{sA} and N_{sD} are eventually present shallow acceptor or donor concentrations which are assumed totally ionized; C_t^* is the contribution of all defect states. The energy diagram, as given schematically in Fig. 1, contains two defect states. These thermally exchange electrons with the conduction or the valence band, according to electron-transition rates which in the case of level A are given by

$$r_{nt\mathrm{A}} = c_{n\mathrm{A}}\, n\,(N_{t\mathrm{A}} - n_{t\mathrm{A}}) - e_{n\mathrm{A}}\, n_{t\mathrm{A}} , \tag{3}$$

$$r_{pt\mathrm{A}} = c_{p\mathrm{A}}\, p\, n_{t\mathrm{A}} - e_{p\mathrm{A}}\,(N_{t\mathrm{A}} - n_{t\mathrm{A}}) . \tag{4}$$

Similar expressions hold for defect state B.

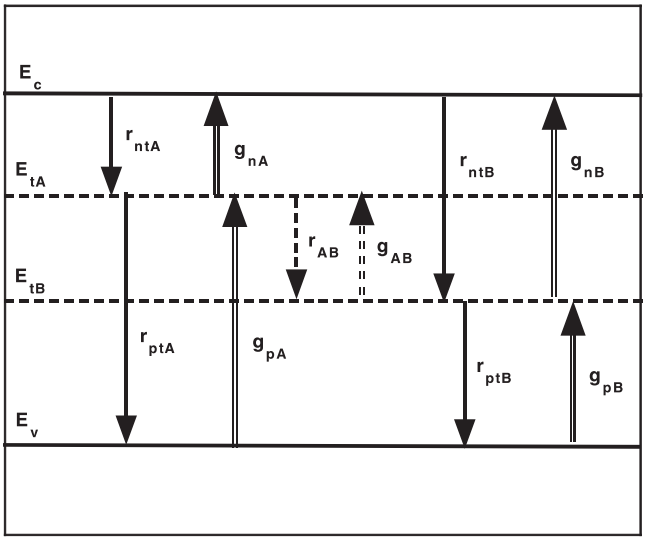

FIGURE 1 Schematic energy-band diagram with conduction-band edge E_{c}, valence-band edge E_{v}, defect-level positions $E_{t\mathrm{A}}$ and $E_{t\mathrm{B}}$, electron-recombination rates $r_{nt\mathrm{A}}$, $r_{pt\mathrm{A}}$, $r_{nt\mathrm{B}}$, $r_{pt\mathrm{B}}$ and r_{AB} and optical generation rates $g_{n\mathrm{A}}$, $g_{p\mathrm{A}}$, $g_{n\mathrm{B}}$, $g_{p\mathrm{B}}$ and g_{AB}

In the Shockley–Read–Hall scheme [18], the capture constant is $c_{n\mathrm{A}} = \sigma_{n\mathrm{A}}\, v_n^{\mathrm{th}}$, where $\sigma_{n\mathrm{A}}$ is the thermal capture cross section and v_n^{th} the electron thermal velocity at temperature T. The electron thermal emission rate is

$$e_{n\mathrm{A}} = g_{\mathrm{A}}\, c_{n\mathrm{A}}\, N_{\mathrm{c}}\, \exp[(E_{\mathrm{c}} - E_{t\mathrm{A}})/kT] , \tag{5}$$

where N_{c} is the effective conduction-band density of states, E_{c} is the conduction-band edge and g_{A} is the defect degeneracy factor. The hole capture constant $c_{p\mathrm{A}}$ and emission rate $e_{p\mathrm{A}}$ are defined accordingly. The optical transition rates between level A and the conduction band and between the valence band and level A are given by

$$g_{n\mathrm{A}} = s_{n\mathrm{A}}\, \Phi\, n_{t\mathrm{A}} , \tag{6}$$

$$g_{p\mathrm{A}} = s_{p\mathrm{A}}\, \Phi\,(N_{t\mathrm{A}} - n_{t\mathrm{A}}) , \tag{7}$$

where Φ is the photon flux at position x, whose spatial dependence is given by (1); $s_{n\mathrm{A}}$ and $s_{p\mathrm{A}}$ are the optical cross sections relative to level A. The corresponding transition rates involving level B are defined accordingly.

Eventual transitions between the two levels A and B can be included according to the equations, written for the case where the relative positions are such that $(E_{\mathrm{c}} - E_{t\mathrm{A}}) < (E_{\mathrm{c}} - E_{t\mathrm{B}})$:

$$r_{\mathrm{AB}} = c_{\mathrm{AB}}\, n_{t\mathrm{A}}\,(N_{t\mathrm{B}} - n_{t\mathrm{B}}) - k_{\mathrm{AB}}\, n_{t\mathrm{B}}\,(N_{t\mathrm{A}} - n_{t\mathrm{A}}) , \tag{8}$$

$$g_{\mathrm{AB}} = \lambda_{\mathrm{AB}}\, \Phi\, n_{t\mathrm{B}}\,(N_{t\mathrm{A}} - n_{t\mathrm{A}}) . \tag{9}$$

Here $c_{AB} = \sigma_{AB}\ v_n^{th}$, where σ_{AB} is an interlevel thermal capture cross section and λ_{AB} is the coefficient which determines the strength of the interlevel optical absorption. The following relation is assumed between the capture coefficient c_{AB} and the coefficient k_{AB}:

$$k_{AB} = \frac{g_B}{g_A}\, c_{AB}\ \exp[(E_{tB} - E_{tA})/kT]\,. \tag{10}$$

This relation expresses that, in thermal equilibrium, the transition rates A to B, and B to A, are equal, i.e. $r_{AB} = 0$, independently of (5), which expresses equilibrium between each level and the bands. In the numerical treatment, the electron concentration n, the hole concentration p, as well as the occupied level concentrations n_{tA} and n_{tB}, are expressed in terms of quasi-Fermi levels F_n, F_p, F_{tA} and F_{tB}, allowing the description for non-equilibrium situations. For non-degenerate semiconductors, one has [15]:

$$n = N_c\ \exp[(F_n - E_c)/kT]\,, \tag{11}$$

$$p = N_v\ \exp[(E_v - F_p)/kT]\,, \tag{12}$$

$$n_{tA} = N_{tA}\,\frac{1}{1 + g_A\ \exp[(E_{tA} - F_{tA})/kT]}\,. \tag{13}$$

The expression for n_{tB} is defined similarly.

The continuity equations for electrons, holes and occupied defects then read

$$\frac{\partial n}{\partial t} = \frac{1}{q}\,\frac{\partial J_n}{\partial x} - r_{ntA} - r_{ntB} + g_{nA} + g_{nB} + g_{bb} - r_{bb}\,, \tag{14}$$

$$\frac{\partial p}{\partial t} = -\frac{\partial J_p}{\partial x} - r_{ptA} - r_{ptB} + g_{pA} + g_{pB} + g_{bb} - r_{bb}\,, \tag{15}$$

$$\frac{\partial n_{tA}}{\partial t} = r_{ntA} - g_{nA} - r_{ptA} + g_{pA} - r_{AB} + g_{AB}\,, \tag{16}$$

$$\frac{\partial n_{tB}}{\partial t} = r_{ntB} - g_{nB} - r_{ptB} + g_{pB} + r_{AB} - g_{AB}\,, \tag{17}$$

where, for reason of completeness, we have added band-to-band recombination terms r_{bb} and optical generation terms g_{bb}. The current densities J_n and J_p are the sums of drift and diffusion terms

$$J_n = q\,\mu_n\,n\,E + \mu_n\,kT\,\frac{\partial n}{\partial x}\,, \tag{18}$$

$$J_p = q\,\mu_p\,p\,E - \mu_p\,kT\,\frac{\partial p}{\partial x}\,, \tag{19}$$

where E is the electric field and μ_n and μ_p are the electron and hole mobilities.

This set of equations describes the steady-state ($\partial/\partial t = 0$) and transient behavior of the microscopic system, once the illumination pattern is given. This latter can be treated by taking a finite number of illumination periods Λ, bordered by non-illuminated regions at the left- and right-hand sides of the structure. Another possibility is to use a super-Gaussian dependence of $I_0(x)$, simulating a beam of finite size [17]. In any case, only the shape of the central periods will be used in the analysis of the photorefractive characteristics.

The as-obtained electric field $E(x)$ is Fourier-analyzed. The zero component yields the applied field. From the first-order Fourier component E_1, the two-wave-mixing gain Γ can be obtained, according to [1–3]

$$\Gamma = \frac{2\pi}{\lambda\cos\theta}\,n_r^3\,r_{41}\,\frac{|E_1|}{m}\,, \tag{20}$$

where n_r is the index of refraction of the medium and r_{41} is the electro-optic coefficient. The gain is defined as negative when electrons are the dominant photocarriers; it is positive when the holes are dominant.

The diffraction efficiency η is defined as

$$\eta = \sin^2\left(\frac{\pi\ \Delta n_r\ L}{\lambda\ \cos\theta}\right)\,, \tag{21}$$

where L is the interaction length and Δn_r is given by

$$\Delta n_r = \frac{1}{2}\,n_r^3\,r_{41}\,|E_1|\,. \tag{22}$$

The numerical solution of the above set of equations is obtained following methods which are standard from the study of electronic devices [15, 19]. After scaling and discretization according to a variable-size mesh, the discretized equations are expressed in terms of the variables ψ, F_n, F_p, F_{tA} and F_{tB}. The use of these variables presents the advantage of dealing with quantities which vary over the same order of magnitudes. This yields for each discretization point a set of five second-order non-linear differential equations. These are linearized in terms of small corrections of the variables to an appropriate initial guess and iterated until desired convergence is achieved. The left and right boundaries x_L and x_R are taken sufficiently far from the illuminated region, such that thermal equilibrium at the contacts can be assumed. When V_{ext} represents the applied voltage, the corresponding boundary conditions are then

$$\psi(x_L) = 0,\ F_n(x_L) = F_p(x_L) = F_{tA}(x_L) = F_{tB}(x_L) = F_0\,, \tag{23}$$

$$\psi(x_R) = -V_{ext},\ F_n(x_R) = F_p(x_R) = F_{tA}(x_R) = F_{tB}(x_R) = F_0 - qV_{ext}\,, \tag{24}$$

where F_0 is the bulk equilibrium Fermi level, which can be obtained from the charge-neutrality condition at the given temperature.

3 Steady-state analysis of InP with two defect levels

The formal developments are applied to InP, a crystal for which numerous experimental results have been published. InP is a direct gap semiconductor with $E_g = 1.35$ eV at room temperature and its electro-optic coefficient at $\lambda = 1.06\,\mu$m, $r_{41} = 1.34$ pm/V, is one of the largest for classical semiconductors. Experimental studies including Deep Level Transient Spectroscopy (DLTS), photoluminescence and electron spin resonance on Fe-doped InP have led to the evidence that Fe introduces a defect state at 0.65 eV below the conduction-band edge, corresponding to the Fe^{2+}/Fe^{3+} state [9]. Multiple defects have been suggested to explain the experimentally observed consequences of electron–hole

competition, such as a change in energy-coupling direction in two-wave mixing. One possible microscopic origin was the excited Fe^{2+*} level at 0.30 eV below the conduction-band edge [20]. In the two-defect-level system, the first level, labeled A, corresponds to the Fe^{2+}/Fe^{3+} acceptor level, for which the microscopic parameters are given in Table 1. They correspond to values as cited in experimental studies [9, 21]. The second level, labeled B, will be considered with free parameters, among which the energy position $E_{t\mathrm{B}}$, the concentration $N_{t\mathrm{B}}$, the thermal capture cross section σ_{B} and the optical cross section s_{B} are the most important ones. Values for most numerical applications are given in Table 1, and are explicitly specified, when modified. Varying their value in a given range allows a systematic study on the effect of the second level on the resulting photorefractive characteristics.

In Fig. 2 we show, together with the illumination pattern, the electric field as a function of position x for the two-defect system (AB) in comparison with the field when the level A alone is present. The illumination period Λ of the sinusoidal illumination pattern is of 4.5 μm, the temperature is $T = 300$ K, the intensity I_0 is 100 mW/cm^2 and the modulation depth is $m = 1$. Calculations have been done on a system consisting of nine illumination periods Λ, separated from the respective limits x_{L} and x_{R} by a distance of 3Λ, which is not illuminated. The number of discretization points was 80 per period. This yields stable numerical solutions and, for the central periods, negligible effects from the borders between the illuminated and the non-illuminated regions. For both systems, the maximum electric field strength occurs in the less-illuminated part of the illumination pattern, the phase shift between the position of the maximum electric field position and of the maximum illumination being different from $\pi/2$, as would be the case in the small-modulation limit. The electric field is stronger by a factor of two in the case of the defect A alone, as compared to the AB case. In both cases, the shape of the electric field is non-sinusoidal. Figure 3 gives the spectral analysis with the normalized Fourier amplitudes. The Fourier analysis implies that the results for the central period are reproduced periodically in both $+x$ and $-x$ directions. The figure shows that the weight of the fundamental component is 0.48 for case A and 0.78 for case AB. Figure 4a shows the concentration profile for the occupied level concentration A, when the level A is alone, and in Fig. 4b, $n_{t\mathrm{A}}(x)$ together with $n_{t\mathrm{B}}(x)$. For the single-defect case, the function $n_{t\mathrm{A}}(x)$ is modulated around its bulk thermal equilibrium value $n_{t\mathrm{A}0} = 1 \times 10^{16}$ cm^{-3}, giving a total charge-concentration profile, having, except for the opposite sign, essentially the same shape as the occupied level concentration $n_{t\mathrm{A}}(x)$. In the two-defect case, we have taken the B level of donor type and with an energy $E_{t\mathrm{B}}$ slightly below that of

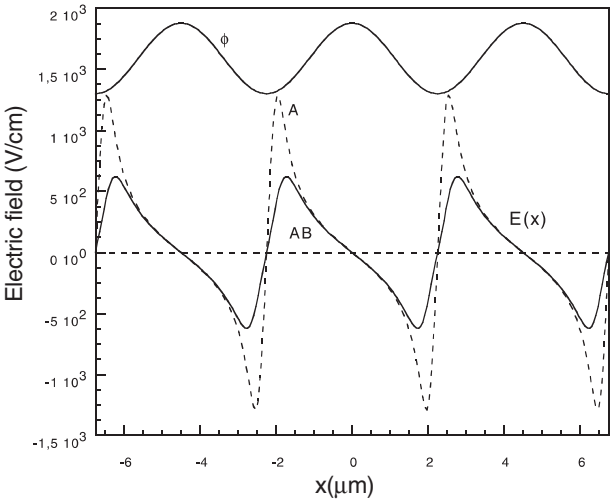

FIGURE 2 Electric field as function of position x, $E(x)$, and illumination pattern $\Phi(x)$ for double-defect configuration AB, with parameter set of Table 1, and the case when only defect level A is present ($N_{t\mathrm{B}} = 0$). The system used for the calculations extends over a total of 15 periods of width Λ, the nine central periods being illuminated, with three non-illuminated periods on each side. The figure shows the three periods in the center of the system

Host material InP	
Energy gap	$E_{\mathrm{g}} = 1.35$ eV
Electron mobility	$\mu_n = 1470$ cm^{2}Vs
Hole mobility	$\mu_p = 150$ cm^{2}Vs
Electron effective mass	$m_{\mathrm{e}}^*/m_0 = 0.08$
Hole effective mass	$m_{\mathrm{h}}^*/m_0 = 0.40$
Electro-optic coefficient	$r_{41} = 1.34$ pm/V
Refractive index	$n_{\mathrm{r}} = 3.29$
Level A (acceptor)	
Energy position	$E_{\mathrm{c}} - E_{t\mathrm{A}} = 0.65$ eV
Concentration	$N_{t\mathrm{A}} = 6 \times 10^{16}$ cm^{-3}
Electron thermal capture cross section	$\sigma_{n\mathrm{A}} = 1.3 \times 10^{-14}$ cm^2
Hole thermal capture cross section	$\sigma_{p\mathrm{A}} = 3 \times 10^{-16}$ cm^2
Electron photo-ionization cross section	$s_{n\mathrm{A}} = 4 \times 10^{-18}$ cm^2
Hole photo-ionization cross section	$s_{p\mathrm{A}} = 3.1 \times 10^{-16}$ cm^2
Level B (donor)	
Energy position	$E_{\mathrm{c}} - E_{t\mathrm{B}} = 0.75$ eV
Concentration	$N_{t\mathrm{A}} = 2 \times 10^{16}$ cm^{-3}
Electron thermal capture cross section	$\sigma_{n\mathrm{A}} = 6.5 \times 10^{-15}$ cm^2
Hole thermal capture cross section	$\sigma_{p\mathrm{A}} = 1.5 \times 10^{-16}$ cm^2
Electron photo-ionization cross section	$s_{n\mathrm{A}} = 3.1 \times 10^{-16}$ cm^2
Hole photo-ionization cross section	$s_{p\mathrm{A}} = 4 \times 10^{-18}$ cm^2
Shallow dopants	
Concentration	$N_{\mathrm{sD}} - N_{\mathrm{sA}} = 10^{16}$ cm^{-3}

TABLE 1 Parameters used in the numerical applications, describing the InP semiconductor, as well as the defect levels A and B. Electron and hole photo-ionization cross sections have been inverted for the case of level B, relative to level A. Band-to-band transition rates r_{bb} and g_{bb} are set equal to zero

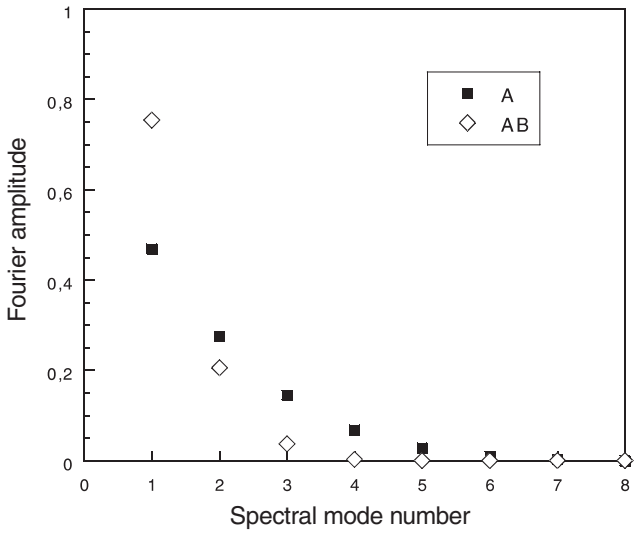

FIGURE 3 Normalized Fourier components for system AB and system A

the first level $E_{t\mathrm{A}}$. The addition of the second level modifies the thermal equilibrium value of $n_{t\mathrm{A}0}$, which is now equal to $1.025 \times 10^{16}\,\mathrm{cm}^{-3}$, and the lower-lying level B is occupied at 98%. The illumination, followed by generation, carrier drift and diffusion and subsequent recombination, creates a defect level occupation for the level A which is completely different from that of the single-defect case. The functions $n_{t\mathrm{A}}(x)$ and $n_{t\mathrm{B}}(x)$ produce a charge-density profile which is illustrated in Fig. 4c. The maximum values of ϱ/q are by a factor of 100 weaker than the values of the corresponding occupied level functions. It should be noted that the resulting function $\varrho(x)$ strongly depends on the various parameters used in the description of the model. Figure 5 shows the various transition rates for generation and recombination. In the final steady-state configuration, the dominant effect on the level

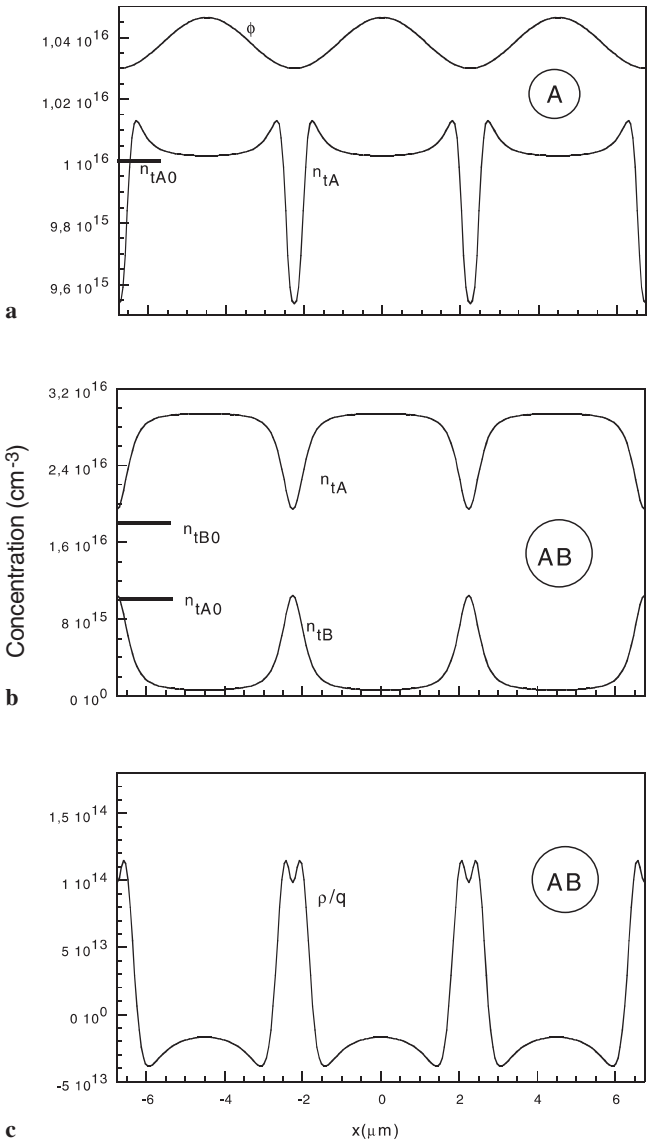

FIGURE 4 **a** Illumination pattern and occupied level concentration $n_{t\mathrm{A}}$ for level A, when concentration of level B is zero; $n_{t\mathrm{A}0}$ is the bulk thermal equilibrium concentration. **b** Occupied level concentrations for levels A and B in system AB. The bulk thermal equilibrium concentrations are respectively $n_{t\mathrm{A}0}$ and $n_{t\mathrm{B}0}$. **c** Charge density ϱ divided by electronic charge q for system AB

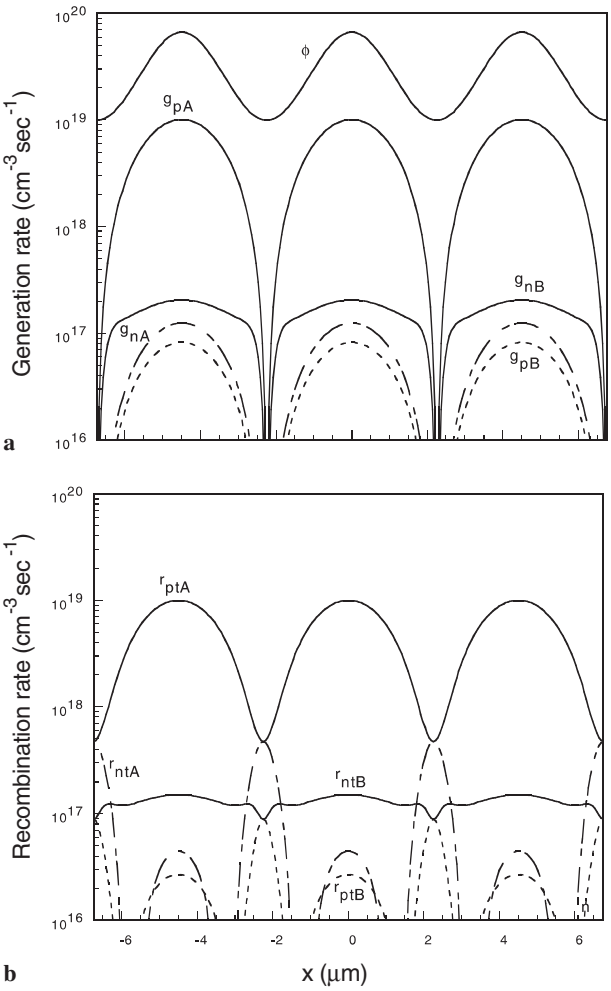

FIGURE 5 **a** Illumination pattern and optical generation rates for system AB as function of position x for transitions $g_{n\mathrm{A}}$, $g_{p\mathrm{A}}$, $g_{n\mathrm{B}}$ and $g_{p\mathrm{B}}$. **b** Recombination rates as function of position x for $r_{nt\mathrm{A}}$, $r_{pt\mathrm{A}}$, $r_{nt\mathrm{B}}$ and $r_{pt\mathrm{B}}$, as defined in Fig. 1

A is the generation from the valence band to level A, followed, for a great part of the carriers, by immediate recombination along the same path. For level B, the major transitions occur between the state $E_{t\mathrm{B}}$ and the conduction band, either by generation or thermal recombination. Part of the photogenerated electrons diffuse to the borders of the illumination period, where they recombine through the A levels. The final carrier and charge-density profiles result from the detailed balance of the generation, recombination and diffusion processes, which explains that a slight modification of one of the parameters can produce profound changes in the charge-density profile.

In the framework of the steady-state analysis, it is possible to determine the effect of one particular parameter, corresponding either to the host crystal, the impurity levels or to the experimental conditions on the resulting quantities, such as the maximum electric field strength E_{m}, the first Fourier component E_1 and the gain coefficient Γ, as defined by (20).

In Fig. 6a we show for the same system E_{m}, E_1 and Γ as functions of the energy position of the second level B, all other parameters being kept constant. The zero value of $E_{t\mathrm{B}}$ corresponds to the valence-band edge. As the figure shows, the evolution of the three quantities goes in parallel. Roughly four distinct regions can be separated. For values of $E_{t\mathrm{B}}$ lower

than 0.4 eV, the three functions under study remain essentially constant with the parameter value $E_{t\mathrm{B}}$. Beyond that region, there is a minimum for $(E_{t\mathrm{B}} - E_{\mathrm{v}}) = 0.50\,\mathrm{eV}$, followed by an increase leading to a constant value from 0.6 to 0.85 eV, and a slightly larger value for $E_{t\mathrm{B}}$ beyond this value of 0.85 eV.

This behavior can be compared with the corresponding evolution as a function of $E_{t\mathrm{B}}$ of the various carrier concentrations n, p, $n_{t\mathrm{A}}$ and $n_{t\mathrm{B}}$, as given in Fig. 6b. These are taken under sinusoidal illumination conditions, at a particular position, namely $x = 0$, i.e. at the maximum illumination. The hole concentration p remains the dominant free carrier. Comparison of Fig. 6a and b shows the four regions in common to all quantities. For $E_{t\mathrm{B}}$ lower than 0.4 eV, $n_{t\mathrm{B}}$ has its maximum value, being even larger than $n_{t\mathrm{A}}$. For $E_{t\mathrm{B}}$ between 0.4 eV and 0.6 eV, there is a transition region where $n_{t\mathrm{B}}$ decreases by two decades, $n_{t\mathrm{A}}$ increasing by about a factor of five. This is followed by a constant value of all quantities for $E_{t\mathrm{B}}$ between 0.6 and 0.85 eV. Beyond this latter value $n_{t\mathrm{B}}$ decreases continuously. This evolution is the combined result of several effects. The modification of the level position $E_{t\mathrm{B}}$ produces a modification of the thermal equilibrium value of the Fermi energy, resulting from the charge-neutrality condition. This in turn determines the thermal equilibrium values of the concentrations n, p, $n_{t\mathrm{A}}$ and $n_{t\mathrm{B}}$ and their corresponding values under illumination. This leads to the final charge-density profile and electric field pattern. The here shown strong dependence on the value of the parameter $E_{t\mathrm{B}}$ also occurs for other parameters used in the description of the system.

In Fig. 7 we show, as functions of the illumination maximum I_0, the values of E_{m}, E_1 and Γ. All three quantities are increasing functions of I_0. It should be noticed that the ratio E_1/E_{m} decreases with I_0; a stronger light intensity produces an increase of the anharmonic character of the space-charge field.

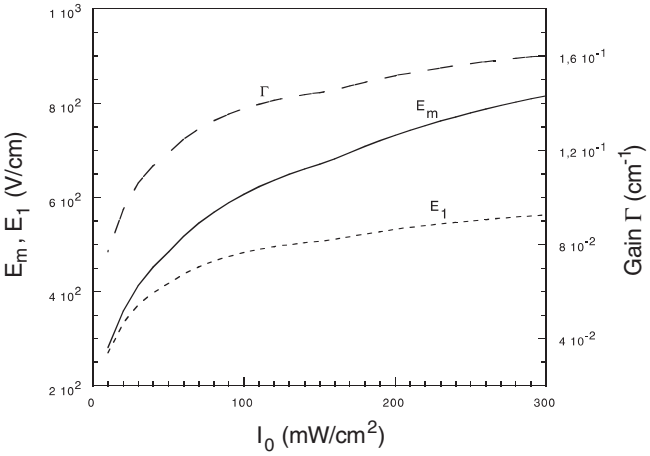

FIGURE 7 Maximum electric field E_{m}, first Fourier component E_1 and gain Γ for system AB, as functions of illumination intensity I_0

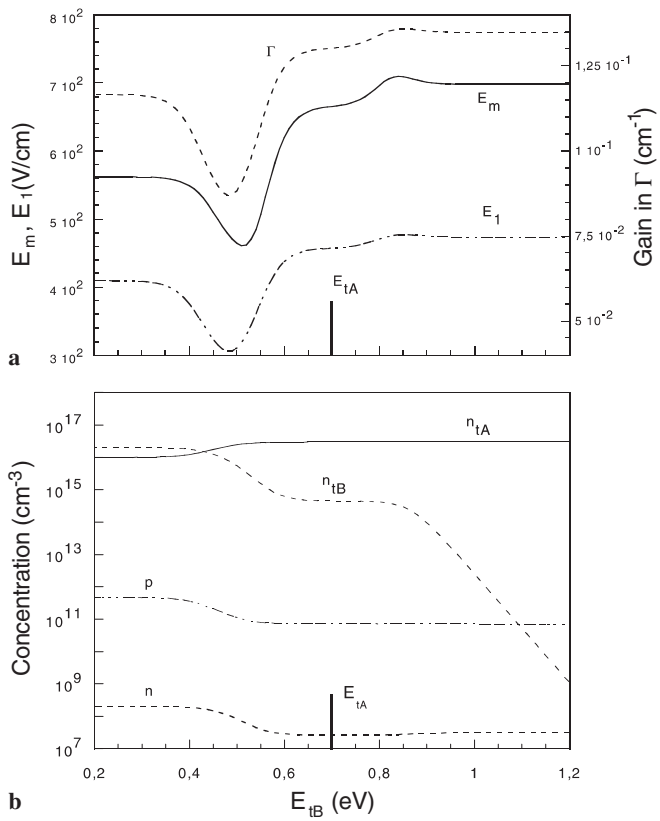

FIGURE 6 **a** Maximum value of the electric field E_{m}, absolute value of first Fourier component amplitude E_1 and two-wave-mixing gain Γ as functions of $E_{t\mathrm{B}}$. Other parameters of the system AB are those of Table 1. **b** Electron concentration n, hole concentration p, level-A occupation $n_{t\mathrm{A}}$ and level-B occupation $n_{t\mathrm{B}}$ at $x = 0$, the maximum of the illumination pattern, as a function of the defect-level position $E_{t\mathrm{B}}$

4 Transient response

From the solution of the full set of basic equations ((2), (14)–(17)), we can obtain the time-dependent variation of all basic quantities such as the electric field and the carrier concentrations. In Fig. 8a, we show, for the configuration studied up to now, the evolution in the extinction case of the space-charge field. The curves show $E(x)$ for different values of t, as indicated in the figure caption. At the instant $t = t_0 = 0$ the illumination is switched from I_0 to zero. In Fig. 8b, we show the corresponding variation of the charge density for x values on one illumination period. The curves show a continuous evolution of $E(x)$ and $\varrho(x)$ up to $t = t_3$, a small modulation at $t = t_4 = 8 \times 10^{-4}$ s, followed by a shape with an inverse sign of the functions, when compared to the steady-state case. In Fig. 9 we show, as functions of t, the evolution of the maximum space-charge field E_{m}, the fundamental component E_1 and the two-wave-mixing gain Γ. In Fig. 9a, corresponding to the extinction case, the evolution of the maximum E field E_{m} shows two regimes which correspond to the two types of field function which appeared in the time-dependent evolution of the charge density. Due to the complexity resulting from the number of recombination processes involving the two defects as well as the conduction and the valence band, it is not in all cases possible to assign the time constant to a well-defined particular process. In the double-defect configuration we have studied here, as can be inferred from Fig. 9b, the first decrease with a time constant around 2×10^{-4} s results from a process where the system tends in a first step to reach electrical neutrality throughout the structure and then evolves towards thermal equilibrium carrier

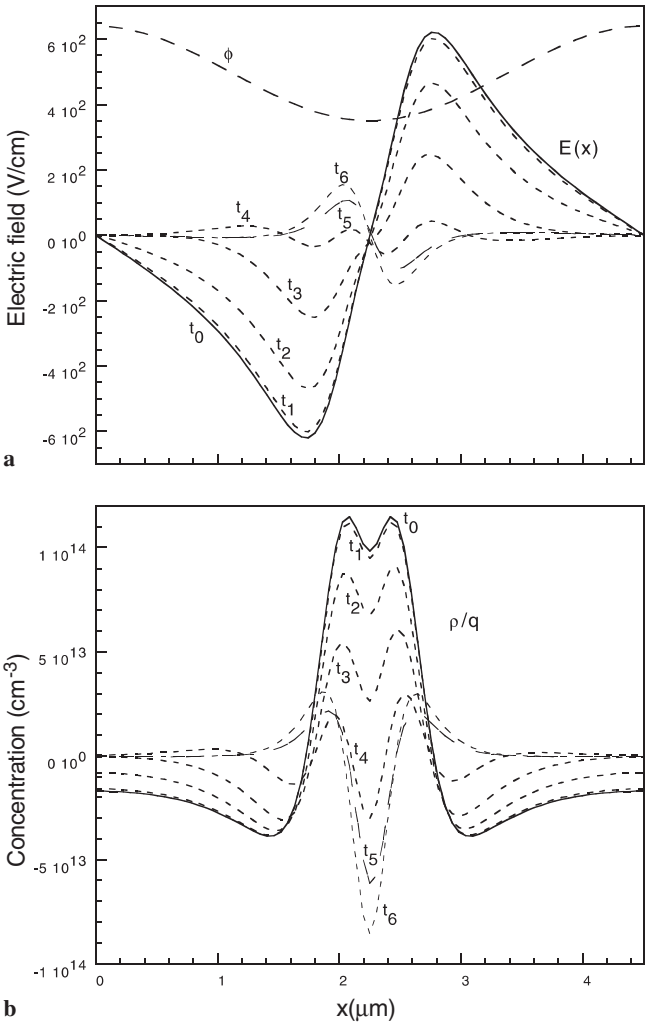

FIGURE 8 **a** Illumination pattern and extinction electric field $E(x)$ for system AB, for x values between $x = 0$ and $x = \Lambda$, for times $t_0 = 0$, $t_1 = 10^{-5}$ s, $t_2 = 10^{-4}$ s, $t_3 = 3 \times 10^{-4}$ s, $t_4 = 8 \times 10^{-4}$ s, $t_5 = 10^{-2}$ s and $t_6 = 6 \times 10^{-2}$ s. **b** Charge density ϱ divided by electronic charge q for same values of t

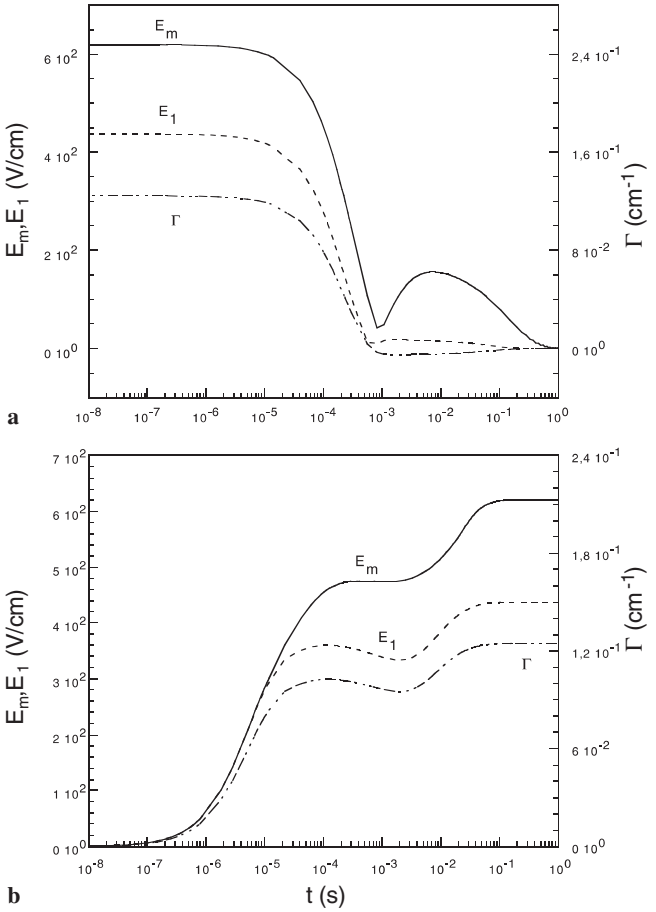

FIGURE 9 **a** Extinction values of maximum electric field E_m, first Fourier component E_1 and two-wave-mixing gain Γ for system AB, with parameters as in Table 1. **b** Time-dependent evolution of same quantities during grating formation

concentrations with, in our case, characteristic time constants of comparable magnitudes for both levels A and B, as can be seen when plotting the time-dependent functions $n_{t\mathrm{A}}$ and $n_{t\mathrm{B}}$. It should be mentioned that the ratio E_1/E_m, which is about 0.7 at steady state, reduces to values of 0.1–0.2 beyond $t = 10^{-3}$ s, a consequence of the highly non-sinusoidal shape of the time-dependent charge density and electric field. Many other shapes of the time evolution of the diffraction grating during extinction may occur, depending on the various parameters involved. A function similar to that shown in Fig. 9a has been observed experimentally in a molecular material where complementary grating competition and bipolar transport was occurring [22]. In Fig. 9b, we show the time evolution of E_m, E_1 and Γ during the writing process. The illumination pattern is switched on at $t = 0$. The shape of all three functions shown is not of the classical exponential type, as is known for the single-defect case. The second defect level is responsible for the undulation around 10^{-3} s.

In Fig. 10 we show, as a function of time, the maximum electric field for two other systems, in addition to the case

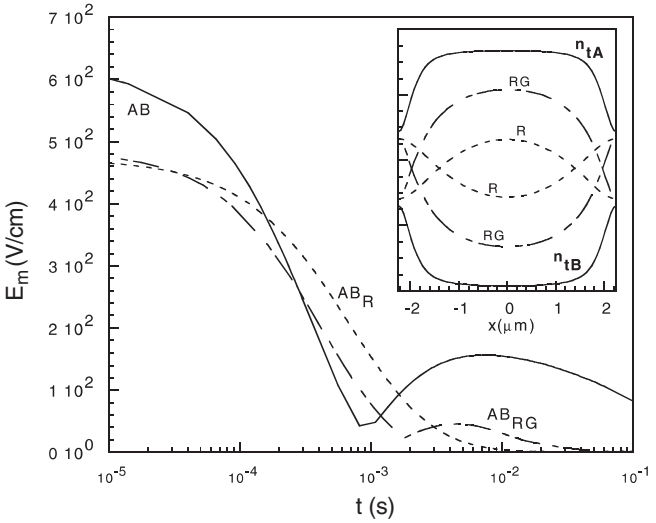

FIGURE 10 Extinction values of maximum electric field E_m for system AB with parameters of Table 1. System $\mathrm{AB_R}$ has the same parameters as AB except that there is a non-zero recombination rate r_{AB} between levels A and B, with $\sigma_{\mathrm{AB}} = 10^{-21}$ cm^2, and curve $\mathrm{AB_{RG}}$ corresponds to system $\mathrm{AB_R}$, plus optical generation between levels A and B, with $\lambda_{\mathrm{AB}} = 10^{-31}$ cm^5. The *inset* shows steady-state occupation of levels A (*three upper curves*) and B (*three lower curves*), for systems AB (*full lines*), $\mathrm{AB_R}$ (*dotted lines*) and $\mathrm{AB_{RG}}$ (*dash-dotted lines*)

AB studied up to now. Label AB_R indicates a system similar to the system AB, but where an interlevel recombination rate r_{AB} has been added; AB_{RG} is system AB_R, but with an additional generation rate g_{AB} between levels A and B. Experimental values of the coefficients σ_{AB} and λ_{AB} are not available. We have chosen $\sigma_{AB} = 10^{-21}$ cm^2 and $\lambda_{AB} = 10^{-31}$ cm^5, which produces the steady-state occupied defect concentrations n_{tA} and n_{tB}, as shown in the inset of Fig. 10. For system AB_R the maximum electrical field E_m decreases uniformly with time, with a time constant of the order of 10^{-3} s. For system AB_{RG}, the additional generation process leads to an increase of the level occupation intermediate between those of the systems AB and AB_R, with a resulting slope of $E_m(t)$ having similarities with the two aforementioned characteristics.

5 Conclusion

In summary, we have included multiple defects in the formal description of the photorefractive effect in semiconducting materials. The resulting set of basic equations can be solved numerically, for any value of the modulation depth m, within the inclusion of all recombination and generation mechanisms to which both levels can give rise. Finding an analytical solution in the general case is impossible, thus requiring use of numerical integration of the basic equations. The numerical procedure allows us to solve exactly the set of equations, once the parameters describing the system and the experimental conditions are given. In particular, one is not restricted to the low-modulation case. When the modulation index m is close to one, the full charge field function $E(x)$ is obtained, from which the fundamental Fourier component can be deduced.

In the application to the photorefractive effect in InP, with two defects, we have shown that it is possible to determine the effect of any parameter describing either the host material, the defects or the experimental conditions on the microscopic quantities of the photorefractive system and on the resulting experimentally accessible macroscopic quantities.

The studied example allows one to stress the existence of a complexity which is far beyond that of the extensively studied single-defect case. The second level leads in a first step to modified thermal equilibrium carrier and occupied level concentrations of the host crystal. This in turn determines the carrier generation and recombination processes, which are basic steps in the formation of the space-charge field. A point to which particular attention should be drawn is that the effect of the second level does not simply add to that of the first one, as if they would act independently. In most cases, there is an interaction between the two levels, either directly or indirectly, at all stages of the grating formation or extinction. The final space-charge field may be the result of the balance between quantities of nearly equal magnitude, whose explicit functions can only be determined from a detailed numerical analysis.

The developments could be extended to systems with more than two defect levels, or to defects leading to a continuous density of states in the semiconducting gap [23]. Application to organic photorefractive materials is also possible, with an appropriate inclusion of all effects occurring in this particular type of materials.

REFERENCES

1 P. Günter, J.P. Huignard: *Photorefractive Materials and their Applications I and II* (Top. Appl. Phys. **61**) (Springer, Berlin 1988)
2 D.D. Nolte: *Photorefractive Effects and Materials* (Kluwer Academic, Boston 1995)
3 L. Solymar, D.J. Webb, A. Grunnet-Jepsen: *The Physics and Applications of Photorefractive Materials* (Clarendon, London 1996)
4 N.V. Kukhtarev: Sov. Tech. Phys. Lett. **2**, 438 (1976)
5 N.V. Kukhtarev, V.B. Markov, S.G. Odulov, M.S. Soskin, V.L. Vinetskii: Ferroelectrics **22**, 949 (1979)
6 M.C. Bashaw, T.P. Ma, R.C. Barker: J. Opt. Soc. Am. B **9**, 1666 (1992)
7 M.C. Bashaw, M. Jeganathan, L. Hesselink: J. Opt. Soc. Am. B **11**, 1743 (1994)
8 F. Jermann, J. Otten: J. Opt. Soc. Am. B **10**, 2085 (1993)
9 R.S. Rana, D.D. Nolte, R. Steldt, E.M. Monberg: J. Opt. Soc. Am. B **9**, 1614 (1992)
10 C. Valley: Appl. Opt. **22**, 3160 (1983)
11 S. Zhivkova, M. Miteva: J. Appl. Phys. **68**, 3099 (1990)
12 P. Tayetbati, D. Mahgerefteh: J. Opt. Soc. Am. B **8**, 1053 (1991)
13 M. Carrascosa, F. Agullo-Lopez: Appl. Opt. **14**, 2851 (1988)
14 A. Shumelyuk, S. Odoulov, G. Brost: J. Opt. Soc. Am. B **15**, 2125 (1998)
15 S. Selberherr: *Analysis and Simulation of Semiconductor Devices* (Springer, Berlin 1984)
16 N. Wolffer, P. Gravey, R. Coquillé: J. Appl. Phys. **78**, 6375 (1995)
17 N. Singh, S.P. Nadar, P.P. Banerjee: Opt. Commun. **136**, 487 (1997)
18 W. Shockley, W.T. Read: Phys. Rev. **87**, 835 (1952); R.N. Hall: Phys. Rev. **87**, 387 (1952)
19 M. Schmeits, A.A. Mani: J. Appl. Phys. **85**, 2207 (1999)
20 P. Delaye, P.U. Halter, G. Roosen: Appl. Phys. Lett. **57**, 360 (1990)
21 G.C. Valley, S.W. McCahon, M.B. Klein: J. Appl. Phys. **64**, 6684 (1988)
22 L. Wang, M.-K. Ng, L. Yu: Phys. Rev. B **62**, 4973 (2000)
23 M. Sakhaf, M. Schmeits: J. Appl. Phys. **80**, 6893 (1996)